JGR Space Physics

RESEARCH ARTICLE
10.1029/2018JA026281

Proton and Electron Injection Path at Geosynchronous Altitude

T. Nagai[1], I. Shinohara[1], H. J. Singer[2], J. Rodriguez[3,4], and T. G. Onsager[2]

[1]Institute of Space and Astronautical Science, Sagamihara, Japan, [2]NOAA Space Weather Prediction Center, Boulder, CO, USA, [3]Cooperative Institute for Research in Environmental Sciences, University of Colorado Boulder, Boulder, CO, USA, [4]NOAA National Centers for Environmental Information, Boulder, CO, USA

Key Points:
- Particle injections proceed during the initial formation of a substorm current wedge at geosynchronous altitude
- Particle injections occur in the limited extent in the premidnight region, the width of which is less than 2 hr in local time
- Proton injections occur even prior to local dipolarization, while electron injections are tightly coupled with local dipolarization in the magnetic field

Supporting Information:
- Supporting Information S1

Correspondence to:
T. Nagai,
nagai@stp.isas.jaxa.jp

Citation:
Nagai, T., Shinohara, I., Singer, H. J., Rodriguez, J., & Onsager, T. G. (2019). Proton and electron injection path at geosynchronous altitude. *Journal of Geophysical Research: Space Physics*, *124*, 4083–4103. https://doi.org/10.1029/2018JA026281

Received 12 NOV 2018
Accepted 22 APR 2019
Accepted article online 29 APR 2019
Published online 13 JUN 2019

Abstract Using tens to hundreds of keV proton and electron flux measurements and simultaneous magnetic field measurements from three Geostationary Operational Environmental Satellites [GOES-13 (75°W), GOES-14 (105°W), and GOES-15 (135°W)], we investigate proton and electron injections and their relationship to the substorm current wedge at geosynchronous altitude. Proton and electron injection processes occur only in the initial formation of the substorm current wedge, the width of which is less than 2 hr in local time in the premidnight region, for moderate substorms. Proton injections are closely related to the formation of a substorm current wedge at geosynchronous altitude, and thus the onset of a substorm, even before local dipolarization in the magnetic field. Proton injections take place only under the western upward field-aligned currents of the current wedge. Electron injections in the energy range of <100 keV are tightly coupled with local dipolarization in the magnetic field, and these take place mostly in the central region of the current wedge, extending in the region under the western upward field-aligned currents.

1. Introduction

The energetic particle injection associated with substorms is one of the most intriguing physical processes, as it can contribute a supply of new particle populations in the inner magnetosphere. Under quasi-steady magnetospheric conditions, energetic particles cannot deeply enter the inner magnetosphere due to their grad B and curvature drift motions in the dipolar magnetic field configuration (e.g., Kivelson & Russell, 1995). Ions move toward the duskside while electrons move toward the dawnside. However, tens to hundreds of keV ions and/or electrons can be transported into the inner magnetosphere from the plasma sheet during substorm-associated magnetic field variations, and this process is called particle injection.

Energetic particle behavior has been studied extensively at the geostationary location of 6.6 R_E (1 R_E is 6,371.2 km) geocentric since the beginning of the space age. Sudden appearances of energetic protons and electrons are observed in association with the onset of a substorm (e.g., Bogott & Mozer, 1973a, 1973b; DeForest & McIlwain, 1971; Erickson et al., 1979; Erickson & Winckler, 1973; Lezniak & Winckler, 1970; Sauvaud & Winckler, 1980; Walker et al., 1976). An excellent review on particle observations and modeling is provided by Thomsen et al. (2001). These energetic particles can be further transported rather impulsively to enter the outer radiation belt inside the geosynchronous altitude (e.g., Friedel et al., 1996; Sergeev et al., 1998; Tang et al., 2018; Turner et al., 2015). It is important to note that the principal variation in the energetic particle flux is a decrease before the onset of a substorm and an increase associated with the onset of a substorm at geosynchronous altitude. This decrease-increase flux behavior is basically understood as the motion of the "particle trapping boundary" associated with the substorm-associated reconfiguration in the magnetic field described below (e.g., Bogott & Mozer, 1973b; Walker et al., 1976). Energetic particle flux usually decreases in a radial direction near the geosynchronous altitude. When particle population moves inward (outward) with adiabatic response according to change in the magnetic field, the flux at a fixed spacecraft position should decrease (increase). Hence, any increase in the particle flux is occasionally a recovery of the flux to its presubstorm level caused by the magnetic field configuration change. This is clearly seen in the highly energetic (MeV) electron flux at geosynchronous altitude (e.g., Nagai, 1982a) where injections of MeV electrons are less frequent. Therefore, simultaneous magnetic field observations are essential for a correct understanding of particle dynamics in the injection process.

Variations in the magnetic field during substorms have also been studied at geosynchronous altitude (e.g., Coleman & McPherron, 1970, 1976; Cummings et al., 1968; Cummings & Coleman, 1968; Kokubun &

McPherron, 1981). Variations in the magnetic field can be well represented by the concept of a substorm current wedge (hereafter, "current wedge") proposed by McPherron et al. (1973). The magnetic field becomes more taillike (stretched) in the growth phase of a substorm, and then becomes dipolar in association with the onset of the expansion phase. The magnetic field gradually returns to its normal (nonsubstorm) condition in the expansion and recovery phases. The effect of field-aligned currents is observed as changes in the east-west component (D) of the magnetic field on the ground at midlatitudes and in space inside of geosynchronous orbit. The eastern downward field-aligned currents produce negative D variations (the westward deflection) and the western upward field-aligned currents produce positive D variations (the eastward deflection) in the Northern Hemisphere.

The magnetic field variations largely depend on the observation point relative to the magnetic equatorial plane. Major variations are a decrease and an increase in the northward component (H) in the magnetic field near the equatorial plane. The magnetic field intensity decreases during the growth phase and increases with dipolarization near the equator. The effect of field-aligned currents is less clear near the equatorial plane. These variations were clearly seen in the magnetic field data from ATS 1 (magnetic latitude of almost zero at 150°W). The magnetic field vector is strongly inclined, along with stronger magnetic field intensity during the growth phase off the equatorial plane. These variations are evident in the magnetic field data at ATS 6 (magnetic latitude of almost 11° at 96°W). Moreover, field-aligned current signatures seen in D have strong seasonal effects due to the dipole tilt effect on the near-tail configuration (e.g., McPherron & Barfield, 1980).

Furthermore, the current wedge expands both westward and eastward in the initial period of several minutes just after an onset at geosynchronous altitude (Nagai, 1982b). The current wedge forms initially in the localized sector (where the local time width is usually less than 1 hr) in the premidnight region. The onset of local dipolarization in both the eastern and westward regions is progressively delayed in the expansion phase of a substorm (see also Nagai, 1987, 1991). Although the fully developed current wedge has the local time extent of more than 6 hr for moderate substorms, a sharp dipolarization of the initial current wedge has its local time width of less than one hour. Outside the initial current wedge, the field becomes further taillike. The localization and evolution of the current wedge have been well established in subsequent studies (e.g., Arnoldy & Moore, 1983; Fairfield et al., 1987; Gelpi et al., 1985; Singer et al., 1985). As a result of the spatial and temporal variations, it is difficult to construct a precise understanding of particle and magnetic field dynamics at geosynchronous altitude with only a single-point observation.

Beginning with the Geostationary Operational Environmental Satellites GOES-13, GOES-14, and GOES-15 series of GOES spacecraft, measurements have been made of energetic (80–800 keV) protons and energetic (30–600 keV) electrons, as well as the magnetic field. GOES-13, GOES-14, and GOES-15 were located near the geographic longitudes of 75°W, 105°W, and 135°W, respectively. The magnetic local time separation of each pair of neighboring satellites is 2 hr, so that observations with these GOES spacecraft enable us to precisely investigate the particle injection processes inside and outside the current wedge. Furthermore, we can identify drifting protons and electrons by comparing flux profiles at two satellite positions. In this study, we identify rapid flux increase events and examine the relationship of particle injections to current wedge formations. A main target of this study is to find the "path" of injection particles into the inner magnetosphere (the outer radiation belt) across geosynchronous altitude. Section 2 introduces the data used in this study. In section 3, event studies reveal the important features of particle dynamics and their relationships with the evolution of the current wedge. Section 4 presents the results of statistical analyses conducted to confirm the important findings in section 3. Section 5 provides the summary and discussion, and section 6 gives the conclusions.

The term "particle injection" is nominally used to mean a particle transport process into the inner magnetosphere from the plasma sheet. However, a particle trapping boundary motion associated with a configuration change in the magnetic field can become dominant at geosynchronous altitude, and can also simultaneously produce flux increases in all energy channels. Moreover, the flux recovery can produce an overshoot of the flux level (e.g., Nagai, 1982a). Attributing any increase in proton and electron flux to any single process is not possible without multipoint three-dimensional particle measurements, but GOES only allows us to have limited 3-D observations. In this study, when the GOES flux clearly exceeds the preevent level and/or the possible quiet-day diurnal level, we consider that the flux increase is due to a particle injection. In other cases, the particle trapping boundary motion may be a dominant process for flux increases,

although we cannot pursue physical processes in the present observations. When flux behaviors in all energy channels for protons and electros look similar, it is possible that flux increases are caused by changes of the magnetic field configuration.

2. Data

We use the data obtained by GOES-13 at 75°W, GOES-14 at 105°W, and GOES-15 at 135°W, although the longitudes of these spacecraft changed slightly (within 1°) during the interval examined in 2016–2017. Here we adopt these values for the satellite positions and use local time as magnetic local time (MLT) for simplicity, as any small differences are not significant for the purposes of this study. The geomagnetic latitude of GOES-13 is 9.4° at its magnetic local midnight at 0500 UT. The geomagnetic latitude of GOES-14 is 8.3° at its magnetic local midnight at 0700 UT. The geomagnetic latitude of GOES-15 is 4.5° at its magnetic local midnight at 0900 UT.

The magnetic field measurements are carried out with time resolution of 0.512 s (Singer et al., 1996). The magnetic field data are presented in the VDH coordinate system (e.g., Kivelson & Russell, 1995). In the VDH system, H (pointing northward) is antiparallel to Earth's dipole axis, D (azimuthal east) is orthogonal to H and a radius vector to the satellite, and V (nearly radial outward) completes the Cartesian coordinate system. Thus, the directions of the H component and D component are the same as those used with ground magnetic field data. We calculate total magnetic field (i.e., magnetic field intensity) B_t and field inclination from the three H, V, and D component values. In this paper, the field inclination is defined as $\mathrm{Inc} = \sin^{-1}(H/B_t)$.

The Energetic Particle Sensor MAGnetospheric Proton Detector provides proton fluxes in five channels (80–110, 110–170, 170–250, 250–350, and 350–800 keV). The time resolution is 16 s for the 80–110-, 110–170-, and 170–250-keV channels, and 32 s for the 250–350- and 350–800-keV channels. The Energetic Particle Sensor MAGnetospheric Electron Detector provides electron fluxes in five channels (30–50, 50–100, 100–200, 200–350, and 350–600 keV). The time resolution is 2 s for the 30–50- and 50–100-keV channels, 4 s for the 100–200-keV channel, 16 s for the 200–350-keV channel, and 32 s for the 350–600-keV channel. We use the flux data from telescopes pointing near the equatorial plane (Jaynes et al., 2013). For statistical analyses, we also use 1-min averaged data.

We use data for the period from 8 April to 17 November 2016, the period from 9 to 23 August 2017, and the period from 1 to 14 December 2017. The magnetic field and particle data are available for the three spacecraft (GOES-13, GOES-14, and GOES-15) for these 226 days. We also examine the GOES-14 and GOES-15 pair data for the period from 15 December 2017 to 17 December 2018. The data from GOES-13 after 15 December 2017 are not available, and the particle observations temporally stopped on 17 December 2018.

The ground magnetic field data are also examined to help interpret the magnetic field variations at geosynchronous altitude. The ground station Fresno (FRN; geomagnetic latitude 43.1°, geomagnetic longitude 304.6°) is located just east of GOES-15 (geomagnetic longitude 297.3°). The ground stations Tucson (TUC; 39.4°, 317.4°) and Boulder (BOU; 47.9°, 322.0°) are located west of GOES-14 (328.3°), and the ground station Stennis (BSL; 39.4°, 340.9°) is located east of GOES-14. The ground station Fredericksburg (47.7°, 354.4°) is located near the GOES-13 meridian (357.6°). Most data plots are found on the website of the World Data Center for Geomagnetism, Kyoto University, and digital (ASCII) data can be obtained from the Time History of Events and Macroscale Interactions during Substorms website. In event studies, a substorm onset timing is determined from the onset of a midlatitude positive bay. The ground-based D variations at midlatitudes can be used to indicate the central meridian of the current wedge (e.g., Clauer & McPherron, 1974), although the direction of the D deflection on the ground may differ from that at geosynchronous altitude (Nagai, 1987). The *AU*/*AL* indices and *Dst* index are examined to determine the condition of magnetospheric disturbances.

3. Event Studies

We first examine the event on 3 October 2016 (section 3.1), when the central spacecraft GOES-14 was located near the center of the current wedge. Second, we examine the events on 5 October and 13 April 2016, when the western spacecraft GOES-15 was located near the center of the current wedge. The event on 13 April

2016 occurred in highly active geomagnetic conditions. Third, we examine the event on 12 August 2016, when the eastern spacecraft GOES-13 was located near the center of current wedge. The center of the current wedge can be determined to be the meridian where there is no *D* deflection in the magnetic field on the ground. At geosynchronous altitude, the center of the current wedge is the region in which a sharp dipolarization starts first with some irregular variations in the *D* component (e.g., Nagai, 1987).

Before proceeding, it is instructive to remember the drift speed of energetic particles at geosynchronous altitude. In a dipole magnetic field, protons drift westward and electrons drift eastward with grad B and curvature of the magnetic field. Protons and electrons with energy of 100 keV and a pitch angle of 90° can travel around Earth at 6.6 R_E with a period of 64 min. Hence, 100-keV protons and electrons can travel the 2-hr local time separation between spacecraft in about 5 min. In examining the 1-min GOES data, the travel time for the 2-hr separation is typically found to be about 2 min for protons in the 80–110-keV channel and electrons in the 100–200-keV channel, as seen in section 4.

It is also instructive to remember "a drifting electron hole" studied by Sergeev et al. (1992). The "drifting hole" is a dropout in the electron flux which drifts eastward from local midnight at a drift speed described above at geosynchronous orbit. This is frequently observed in a certain energy range associated with electron injections. This can be interpreted as follows: energetic electrons have adiabatic response to slow changes in the magnetic field. During the growth phase, the magnetic field becomes stretched on the nightside so that the magnetic field lines move tailward. As the magnetic field intensity at the equatorial plane decreases with the field configuration change, trapped energetic electrons move earthward to conserve the first adiabatic invariant. When the field becomes dipolar in the limited local time sector at the onset of a substorm and electrons are not yet highly energized, the magnetic field lines with a low energetic electron flux are carried into the dipolarization sector. As electrons are transported from the western region as drift motion, a "flux dropout" can be detected east of the dipolarization sector. Formation of the "flux dropout" depends on the radial flux gradient of trapped energetic electrons, and the drifting holes are mostly observed in high-energy (>100 keV) electrons.

3.1. The 3 October 2016 Event

On 3 October 2016, the start of an isolated substorm was identified with the onset of a midlatitude positive bay occurring at 0503 UT (see Figure S1 in the supporting information). There are at least double onsets at 0503 and 0509 UT in the ground magnetic field data, and these double-onset signatures are more evident in the eastern region (FRD). For this substorm, AL reaches −500 nT. The *D* deflection is negative at eastern ground stations FRD and BSL and positive at western ground station FRN. The positive bay signature is evident in *H*, but no significant *D* deflection occurs in the first 20 min after the onset at central ground stations BOU and TUC. These ground magnetic field variations indicate that the central meridian of the current wedge is located near the GOES-14 meridian.

Figure 1 presents the magnetic field data, electron flux data, and proton flux data for the period of 0400–0700 UT from GOES-15, GOES-14, and GOES-13. For electrons, data from the five channels (e1–e5 in the figure, 30–600 keV) are presented. For protons, data from the lower three channels (p1–p3 in the figure, 80–250 keV) are presented. This presentation provides an overview of the event as any changes in the magnetic field and particle fluxes are not easily discernible in a short time interval data set. GOES-14 is located at the 22 MLT meridian at 0500 UT, and observes sharp dipolarization in the magnetic field. A significant decrease in *H* prior to the onset is recovered by a sudden increase in *H* associated with the onset. *D* shows negative and positive variations. There are high-frequency variations in all magnetic field components. These are typical signatures in the center of the current wedge at geosynchronous altitude. The localization of the initial current wedge is evident in magnetic field variations at the eastern GOES-13 and western GOES-15 positions. GOES-13 observes a negative *D* deflection, while GOES-15 observes a positive *D* deflection. A local dipolarization in the magnetic field is delayed at GOES-13. GOES-15 observes a significant decrease in B_t (magnetic field intensity) after the onset. This is a well-known magnetic signature west of the current wedge. The decrease in B_t is interpreted by the diamagnetic effect of injected protons in the evening sector (e.g., Erickson & Winckler, 1973; Lezniak & Winckler, 1970). Double-onset increases are found in the electron and proton fluxes. Since there is no substorm activity prior to 0500 UT on 3 October 2016, the normal flux levels can be easily defined. It is reasonably judged that substorm-associated injections occur for 30–200-keV electrons and 80–250-keV protons.

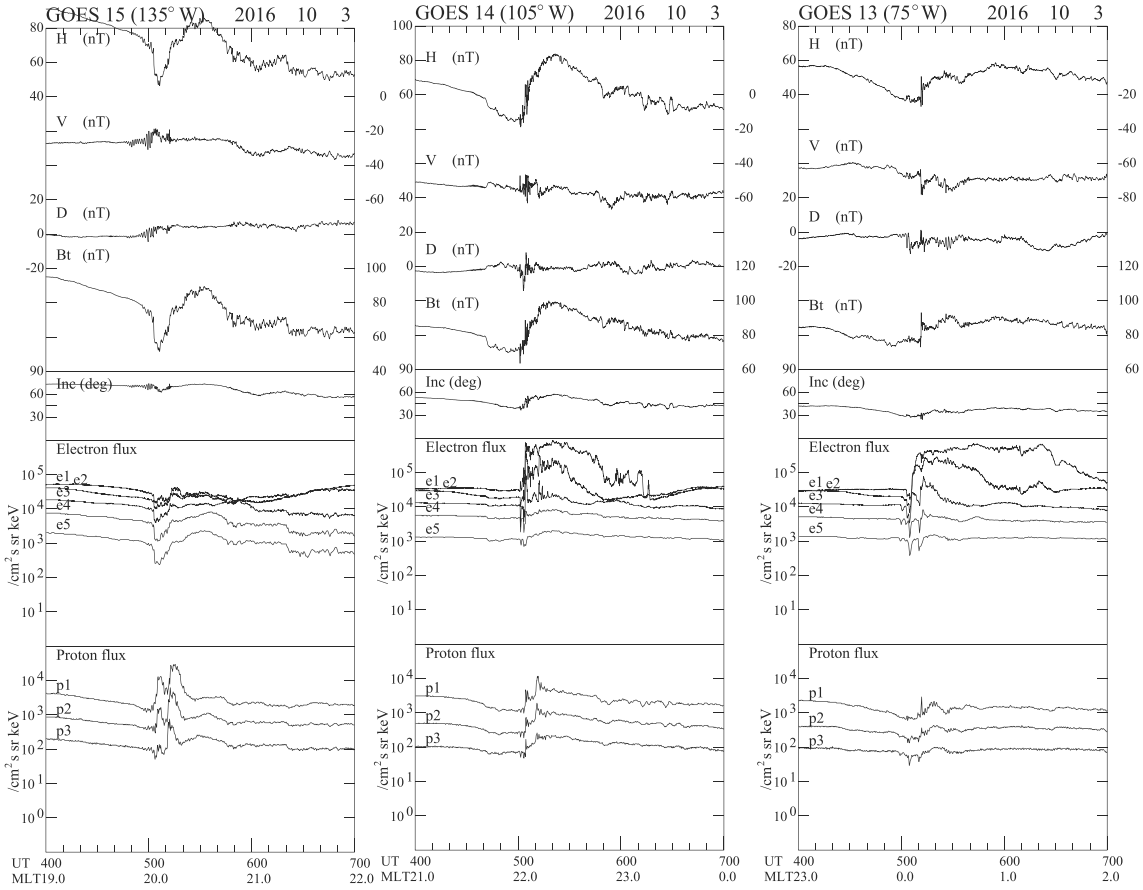

Figure 1. The magnetic field, 30–50-, 50–100-, 100–200-, 200–350-, and 350–600-keV electron fluxes (e1–e5), and 80–110-, 110–170-, and 170–250-keV proton fluxes (p1–p3) at GOES-15, GOES-14, and GOES-13 for the period of 0400–0700 UT on 3 October 2016. The 3-s averaged magnetic field data are used for this plot.

Figure 2 presents the 30-min time interval data for the period of 0455–0525 UT. At GOES-14, initial variations start at 0501 UT in the magnetic field and particles, and sharp dipolarization with a positive *D* deflection occurs at 0504 UT, which likely corresponds to the first onset (0503 UT, this timing is indicated by vertical dashed lines in all panels of the figure) of the double-onset signature. At GOES-13 (at 00 MLT), *D* shows a negative deflection without any clear dipolarization signature just after 0504 UT. Increase in the electron fluxes are observed with some delays (1.5 min) relative to those at GOES-14, while variations are negligible in the proton fluxes. Prior to the electron flux increases at GOES 13, there is a delayed "drifting holes" signature. At GOES 15, proton fluxes increase after 0504 UT, while the electron fluxes decrease in association of the depression in the magnetic field intensity (B_t).

For the second onset in the double-onset signature, small but sharp dipolarization is seen with a positive *D* deflection at GOES-13 (near the midnight meridian). The electron enhancement is evident in the 100–200-keV electron channel and there is a small flux peak in the 80–110-keV proton channel. Flux increase seen in the electron fluxes at GOES-14 is probably due to the expanded dipolarization in the magnetic field. Protons show time dispersion at GOES-14 and GOES-15. It is noted that the flux behaviors in the 30–50- and 50–100-keV electron channel are quite different from those in the >100-keV electron channels at both GOES-14 and GOES13. The high flux state continues for a longer time period for lower energy electrons. This is common in electron observations (e.g., Erickson et al., 1979). It is likely that electrons in the plasma sheet are energized and supplied continuously.

In summary, this substorm starts with two major onsets and double injections occur in different MLT meridians. Proton and electron injections are observed only at one spacecraft position near the center of the current wedge, while drifting electrons or protons are observed the 2-hr west or east meridian.

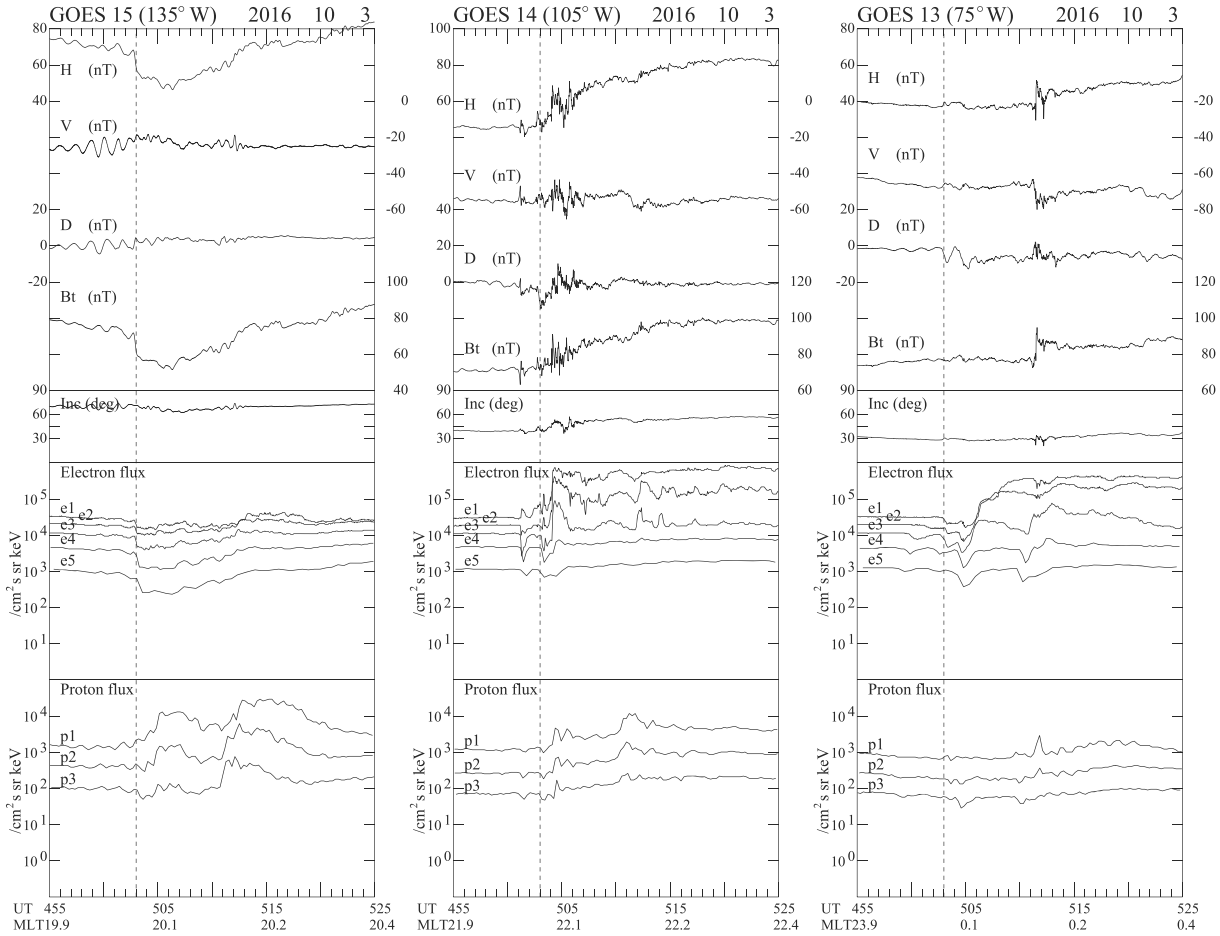

Figure 2. The magnetic field, 30–50-, 50–100-, 100–200-, 200–350-, and 350–600-keV electron fluxes (e1–e5), and 80–110-, 110–170-, and 170–250-keV proton fluxes (p1–p3) at GOES-15, GOES-14, and GOES-13 for the period of 0455–0525 UT on 3 October 2016. Vertical dashed lines at 0503 UT mark the first onset of a double-onset substorm on the ground.

3.2. The 5 October 2016 Event

On 5 October 2016, the start of an isolated substorm was identified with the onset of a midlatitude positive bay occurring at 0714 UT (see Figure S2 in the supporting information). For this substorm, *AL* reaches −500 nT. The *D* deflection is negative at all ground stations from FRN to FRD, although the negative *D* deflection starts later at FRN. The positive bay is sharp at western ground station FRN. These ground magnetic field variations indicate that the central meridian of the current wedge is located near GOES-15.

Figure 3 presents the magnetic field data, electron flux data, and proton flux data for the period of 0600–0900 UT from GOES-15, GOES-14, and GOES-13. GOES-15 observes a sharp dipolarization in the magnetic field and the electron and proton flux increases for this substorm. GOES-14 and GOES-13 also observe dipolarization in the magnetic field, but the variations are more gradual. Electrons show flux increases, while protons do not show any clear changes in the fluxes. Before the onset of this substorm, the low-energy (30–50 and 50–100 keV) electrons show flux increases after 0620 UT until the onset at GOES 14 and GOES 13, probably because the inner edge of the plasma sheet moves earthward and reaches geosynchronous orbit. This signature is often seen in low-energy (<75 keV) electrons (for example, see Thomsen et al., 2001).

Figure 4 presents the data for the period of 0700–0730 UT. At GOES-15, the positive *D* deflection starts at 0714 UT, which corresponds to the ground onset (this timing is presented in all panels of the figure), and sharp dipolarization in the magnetic field starts at 0719.5 UT. During the local dipolarization, *D* becomes slightly negative. Sharp electron flux increases take place in the three low-energy (<200 keV) channels with this local dipolarization. Electron flux increases in the high-energy (>200 keV) channels start slightly earlier,

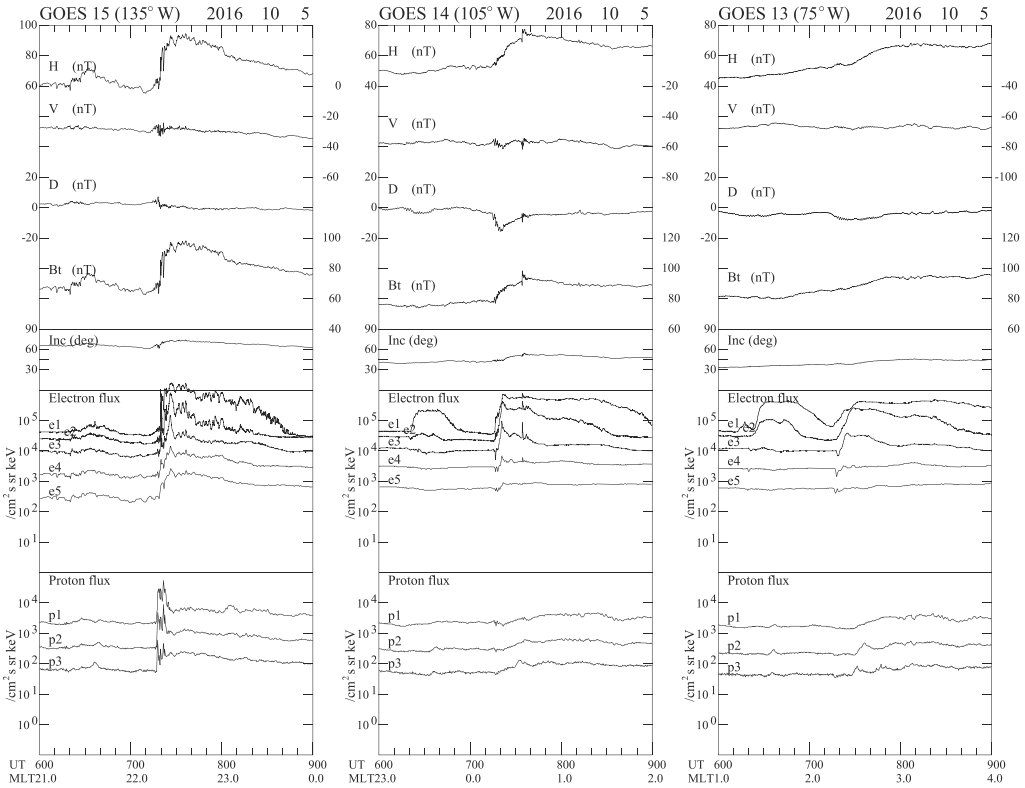

Figure 3. The magnetic field, 30–50-, 50–100-, 100–200-, 200–350-, and 350–600-keV electron fluxes (e1–e5), and 80–110-, 110–170-, and 170–250-keV proton fluxes (p1–p3) at GOES-15, GOES-14, and GOES-13 for the period of 0600–0900 UT on 5 October 2016. The 3-s averaged magnetic field data are used for this plot.

and the flux variations appear to trace the variations in B_t. Proton flux increases start at 0717 UT before the local dipolarization, and these are not associated with any magnetic field variations.

At GOES-14, the negative *D* deflection starts at 0715 UT. Sharp electron flux increases in the two low-energy (30–100 keV) channels start at 0716.5 UT, and are apparently associated with rapid changes in the magnetic field. Electrons in the high-energy (>200 keV) channels show drifting holes and then gradually increase. The low-energy electron increases at GOES-14 almost coincide with the proton increase at GOES-15, and clearly precede the low-energy electron increases at GOES-15. Any injected electrons at GOES-14 cannot move toward GOES-15, opposite the drift motion. As the initially narrow current wedge expands both westward and eastward, this suggests that the low-energy electron increases are variations associated with delayed local dipolarization at the GOES-15 local time.

It is difficult to determine the correct timing for any variation in the magnetic field at GOES-13. Since the timing of local dipolarization coincides with the maximum *D* deflection in the statistical results (e.g., Nagai, 1987, 1991), it is estimated to be 0728 UT at GOES-13 (see Figure 3). The start time of the negative *D* deflection is probably 0714 UT at GOES-13. Electron fluxes gradually start to increase near 0718 UT, although there are drifting holes with "energy dispersion" in the three high-energy channels. An important point here is that electron fluxes increase without any significant magnetic variations. Protons do not show any significant variations by 0730 UT at GOES-14 and GOES-13.

In summary, electron flux increases are observed at the local onset while proton flux increases are observed before the local onset near the center of the current wedge. Electrons show drift motions and appear much faster than the westward expansion of the current wedge under the eastern downward field-aligned currents of the current wedge.

3.3. The 13 April 2016 Event

On 13 April 2016, the start of an isolated substorm was identified with the onset of a midlatitude positive bay occurring at 0613 UT (see Figure S3 in the supporting information). The *D* deflection is negative at FRD and

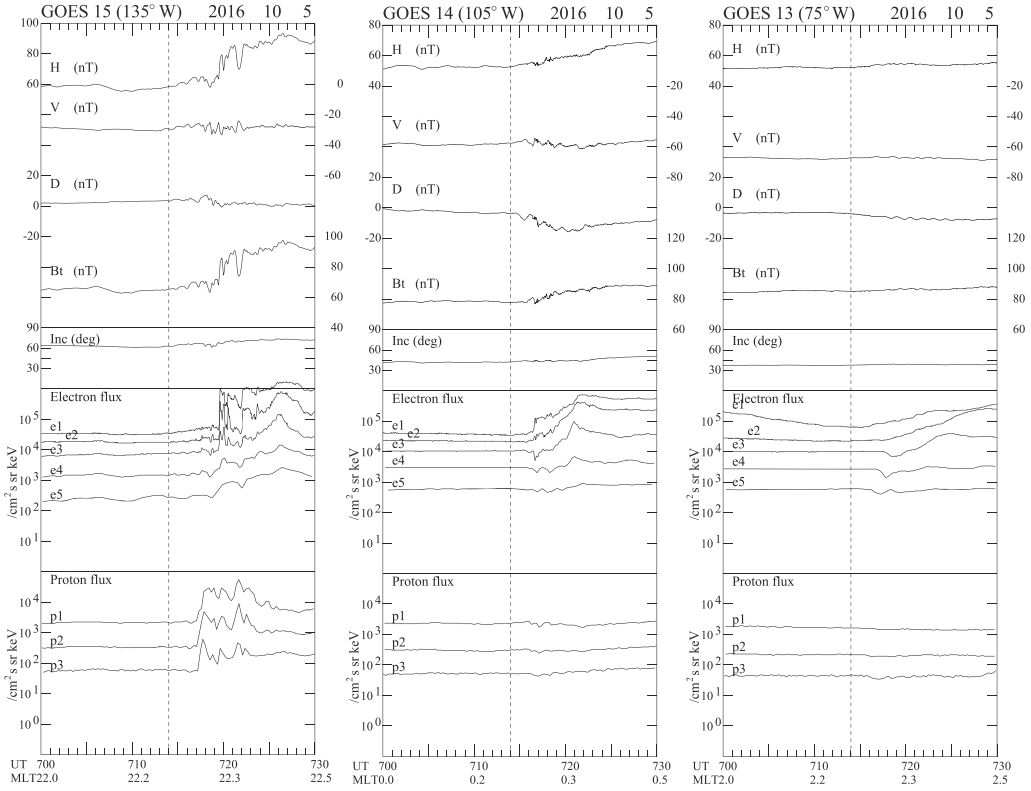

Figure 4. The magnetic field, 30–50-, 50–100-, 100–200-, 200–350-, and 350–600-keV electron fluxes (e1–e5), and 80–110-, 110–170-, and 170–250-keV proton fluxes (p1–p3) at GOES-15, GOES-14, and GOES-13 for the period of 0700–0730 UT on 5 October 2016. Vertical dashed lines at 0714 UT mark the onset of a substorm on the ground.

BSL. *D* does not show any deflection at BOU and TUC, while *D* shows a positive deflection at FRN for the initial 15 min. For this substorm, the *AL* index becomes approximately −400 nT (including a short-lived peak of −800 nT), but elevated geomagnetic activity with *AL* of −300 nT continues prior to this substorm (visit the WDC-C2 website for the related data not shown here). This event demonstrates flux variations due to a particle trapping boundary. Given our focus on flux variations near the onset timing, we show data for the period of 0600–0630 UT in Figure 5. Figure S4 in the supporting information presents the data for the period of 0000–0800 UT.

It is important to note that the magnetic field is highly stretched (more taillike) before the onset of this substorm. The field inclination is a good parameter for the field configuration. The inclination is less than 20° at GOES-14 and GOES-13, and 30° at GOES-15 in the prolonged time before the onset of this substorm. In contrast, the inclination of the quiet day magnetic field taken on 11 April 2016 is 70° for GOES-15, 55° for GOES-14, and 50° for GOES-13 during the midnight hours. The magnetic field intensity is also high compared with the values in the events on 3 and 5 October 2016. The electron and proton fluxes are significantly below the quiet-day nightside levels. The proton fluxes become almost the background level before the onset of this substorm.

At GOES-15, dipolarization in the magnetic field starts at 0613 UT and the *D* deflection is mostly positive. At GOES-14, local dipolarization starts at 0614 UT (evidently with about 1-min delay in comparison) and the *D* deflection is negative. At GOES-13, local dipolarization starts at 0620 UT. *D* shows a positive deflection after 0613 UT and a negative *D* deflection during the local dipolarization. It is important to note the field configuration change in dipolarization for the GOES-14 and GOES-13 locations. The magnetic field intensity increases during the growth phase and then decreases during the local dipolarization. The magnetic field intensity is higher than the quiet-day level even after dipolarization. These are typical magnetic field variations off the equatorial plane. The magnetic field intensity decreases for the 3 October 2016 event and does not change significantly for the 5 October 2016 event at GOES-14 and GOES-13. The center of the current

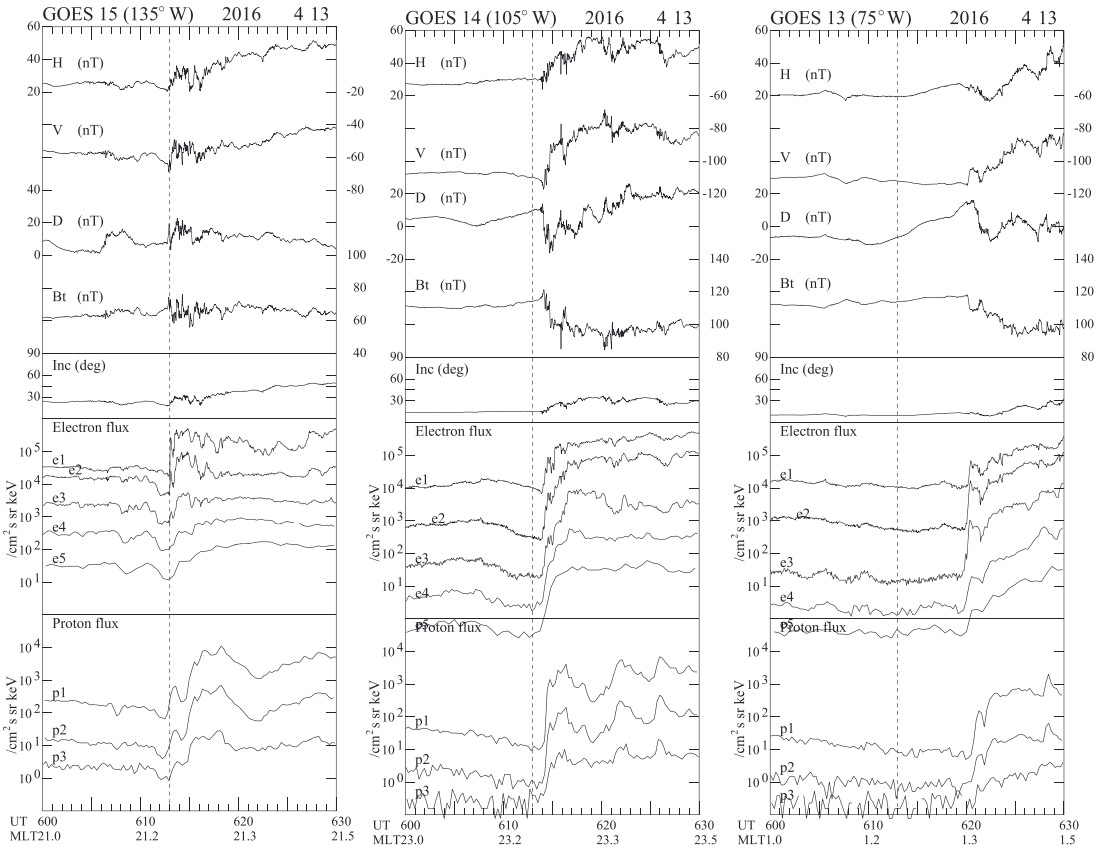

Figure 5. The magnetic field, 30–50-, 50–100-, 100–200-, 200–350-, and 350–600-keV electron fluxes (e1–e5), and 80–110-, 110–170-, and 170–250-keV proton fluxes (p1–p3) at GOES-15, GOES-14, and GOES-13 for the period of 0600–0630 UT on 13 April 2016. Vertical dashed lines at 0613 UT mark the onset of a substorm on the ground.

wedge is located between GOES-15 and GOES-14, and the current wedge expands eastward. The positive *D* change before the negative *D* variations at GOES-13 is probably due to the current sheet crossing in the highly stretched field configuration (see Nagai et al., 1987, 1990).

Both proton flux and electron flux are significantly below the quiet-day nightside levels, and the higher-energy particle flux is almost at the background level before the onset. At GOES-15, the low-energy electrons increase sharply in association with the local onset at 0613 UT. Higher-energy (>200 keV) electrons and protons increase more gradually after 0613 UT, although peak fluxes do not exceed the possible diurnal flux level. All fluxes in the proton and electron channels increase almost simultaneously, and the timing coincides with local dipolarization in the magnetic field at GOES-14 and GOES-13. The flux levels just after the sharp increase are less than the possible diurnal level. There is a 6-min delay between the GOES-14 increase and the GOES-13 increase. This value is longer than the expected 2-min travel time of drift motion.

In summary, the proton flux changes are quite similar to the electron flux changes for local dipolarization under the eastern downward field-aligned currents of the current wedge for the highly stretched field configuration. The flux increases are likely caused by the motion of the particle trapping boundary.

3.4. The 12 August 2016 Event

On 12 August 2016, a substorm started at 0205 UT. A positive bay signature is seen only at FRD and BSL, and a *D* deflection is positive at FRD, BSL, BOU, and FRN (see Figure S5 in the supporting information). Figure 6 presents the magnetic field data, electron flux data, and proton flux data for the period of 0150–0220 UT from GOES-15, GOES-14, and GOES-13.

GOES-13, which is located at the 21.1 MLT meridian, observes a positive *D* deflection starting at 0205 UT (this timing, corresponding to the ground onset, is presented by vertical dashed lines in the figure). Local

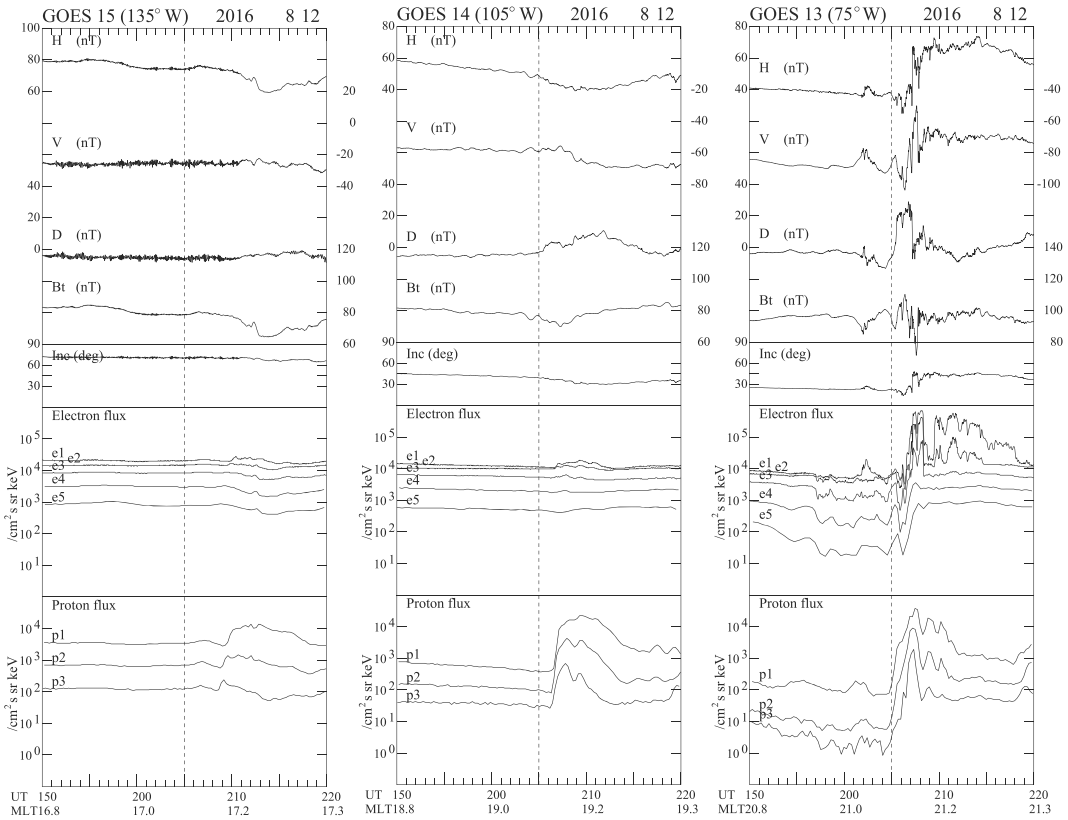

Figure 6. The magnetic field, 30–50-, 50–100-, 100–200-, 200–350-, and 350–600-keV electron fluxes (e1–e5), and 80–110-, 110–170-, and 170–250-keV proton fluxes (p1–p3) at GOES-15, GOES-14, and GOES-13 for the period of 0150–0220 UT on 12 August 2016. Vertical dashed lines at 0205 UT mark the onset of a substorm on the ground.

dipolarization starts at 0207 UT in the magnetic field and electron flux increases are observed simultaneously. Proton flux increases start at 0205 UT, coinciding with the ground onset, rather than local dipolarization in the magnetic field. Since the proton fluxes exceed and then return to the flux levels prior to the substorm (e.g., flux level of 10^3 $cm^{-2}{\cdot}s^{-1}{\cdot}sr^{-1}{\cdot}keV^{-1}$ for the 80–110-keV channel at 00 UT on 12 August 2016), the flux increases are attributed to proton injections.

GOES-14 near the 1900 MLT meridian observes drifting protons after 0206 UT, and GOES-15 near the 1700 MLT meridian observes drifting protons after 0208.5 UT. Higher-energy (170–250 keV) protons arrive at the spacecraft first and the duration of the flux enhancements become slightly longer. However, high flux duration does not change significantly, suggesting that proton injections occur only near GOES-13.

3.5. The Proton Injection Events

Figure 7 shows the proton injection events observed at GOES-14 and GOES-15. The data are shown only in the limited time interval that emphasizes the timing of proton enhancement. An examination of the long-term trend of proton data (not shown here) indicates that these proton enhancements are likely proton injections, not recoveries to the preevent level.

GOES-14 (at magnetic latitude of 8.3°) observed proton flux enhancements with a clear positive *D* deflection after 0413.5 UT on 28 May 2016. Start of Pi2 pulsations, indicating the onset, is recorded around 0413.5 UT at FRD and BOU (not shown here). The field becomes further inclined and the electron fluxes decrease during the proton flux enhancement. Local dipolarization in the magnetic field occurs and the electron flux increases after 0415.5 UT (this timing is presented by vertical dashed line).

GOES-15 (at magnetic latitude of 4.5°) observed proton flux enhancements before 0750 UT and local dipolarization in the magnetic field after 0750 UT on 10 October 2016. This is confirmed with the 16-s proton data

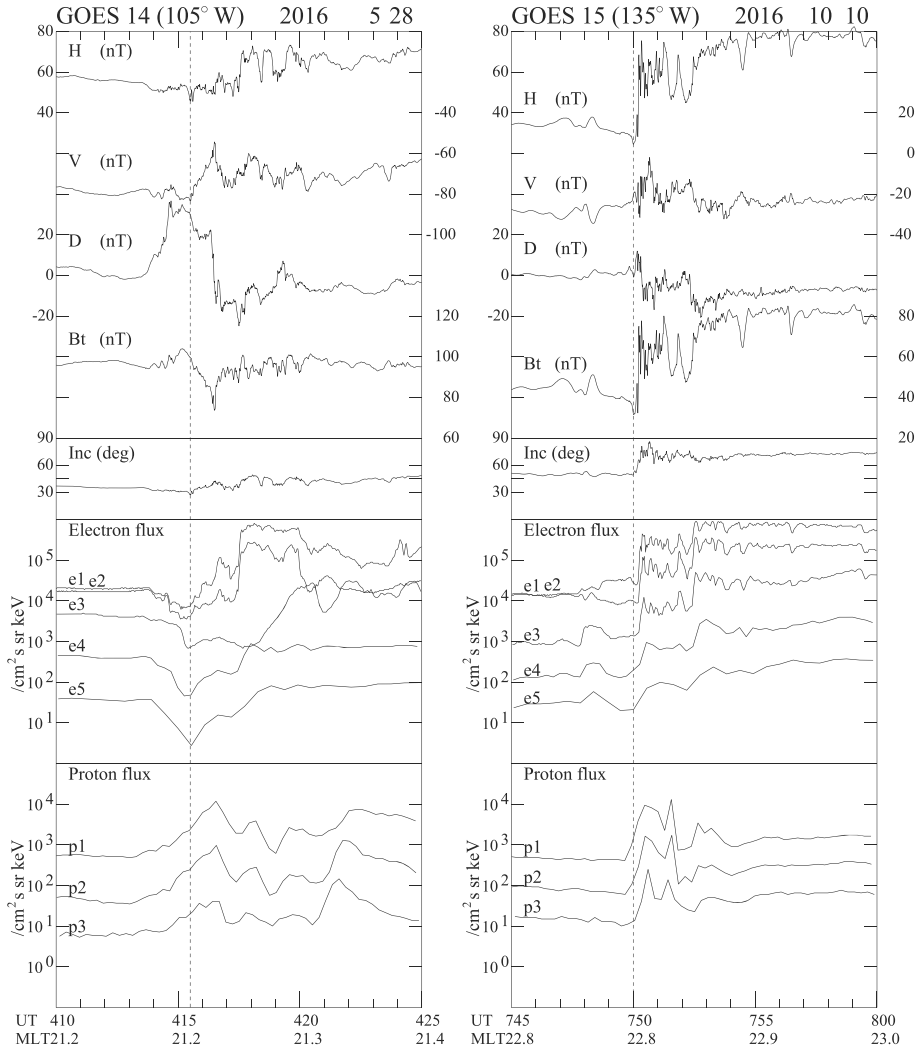

Figure 7. The magnetic field, 30–50-, 50–100-, 100–200-, 200–350-, and 350–600-keV electron fluxes (e1–e5), and 80–110-, 110–170-, and 170–250-keV proton fluxes (p1–p3) at GOES-14 for the period of 0405–0425 UT on 28 May 2016 (left) and at GOES-15 for the period of 0740–0800 UT on 10 October 2016 (right). Vertical dashed line at 0415.5 UT (left) and that at 0750 UT (right) mark local dipolarization at GOES 14 and that at GOES-15, respectively.

and 0.512-s magnetic field data. The electron flux increases are associated with local dipolarization in the 2-s electron data. This event provides much information. The *D* deflection is first positive and then becomes negative. The positive *D* deflection occurs during dipolarization in the field. Hence, it is unlikely that the positive and negative *D* changes are caused by a crossing of the field-aligned current of the current wedge. Indeed, the inclination of the magnetic field is 50° at its minimum, and the particle fluxes are not low. This is a typical example for the irregular *D* variations in the center of the current wedge (e.g., Nagai, 1987).

3.6. Summary of Event Studies

We have presented representative examples of electron and proton flux increases with multiple-satellite observations in 2016–2017. There is local time separation of 2 hr for the pair of two spacecraft. The particle injection is observed from only one spacecraft position, and particle flux increases at other spacecraft positions are attributable to the arrival of drifting particles or the particle trapping boundary motion. The proton injection that often takes place before local dipolarization is found in the center of the current wedge, in which a positive *D* deflection is detected during the event. Low-energy (<100 keV) electron flux increases are well associated with local dipolarization in the magnetic field. As these characteristics are common at GOES-15, GOES-14, and GOES-13, any possibility of spacecraft latitude effects can be eliminated.

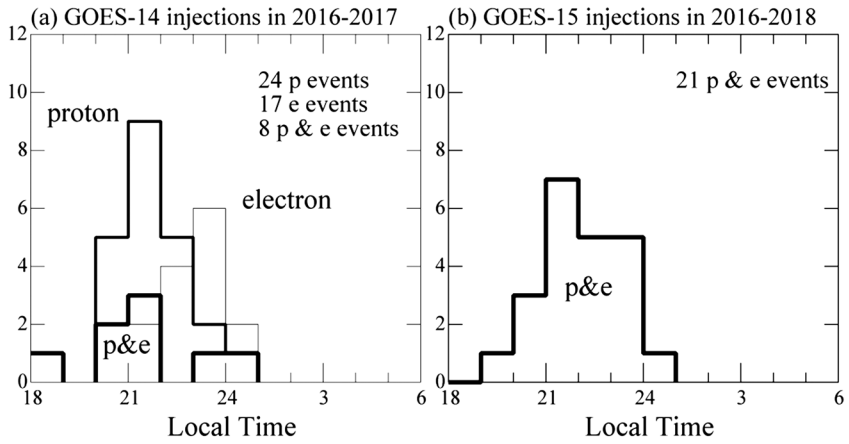

Figure 8. (a) Local time dependence of rapid 80–110-keV proton flux increase events and that of rapid 100–200-keV electron flux increase events from GOES-14. (b) Local time dependence of proton and electron injection events from GOES-15.

4. Statistical Studies

We conduct statistical studies to find the general characteristics of the current wedge/particle injection events and confirm the important findings of the event studies described in section 3. Although it is not easy to define "injection" unambiguously in the data used here, we adopt several criteria for selecting clear injections. The major criterion is that the flux well exceeds the threshold level. Here the threshold level is defined as the flux value near the dusk meridian on each day. The flux value is determined with the data over 17–19 MLT (00–02 UT for GOES-14) preceding selected events. Furthermore, we exclude any possible flux overshoot associated with a trapping boundary motion. In the first step, we select rapid flux increase events in both proton flux and electron flux at GOES-14. We use the 1-min averaged 80–110-keV proton flux data and the 1-min averaged 100–200-keV electron flux data for the 00–12 UT time period for 226 days in 2016–2017. A rapid flux increase is defined as an increase by a factor of 2 within 1 min. When one event is identified, we do not select any events during the following 10-min period to avoid including continuous variations during multiple-onset substorms (e.g., Nagai et al., 1983). This definition covers the flux increase events in section 3 and selects all prominent events found by visual inspection in all one-day data plots. We find 403 proton increase events and 410 electron increase events. In the second step, we select events in which the flux exceeds twice the threshold level within 10 min and the flux does not drop below 0.01 × the threshold value prior to the increase. The latter process is used for excluding a trapping boundary motion. We find 162 proton events and 107 electron events. In the third step, we select events in which GOES-14 observes any flux increase earlier than GOES-13 and GOES-15. In this process, we visually examine a 40-min three-spacecraft data plot for each event. In this process, we examine original high-time resolution particle data, if necessary, and we find a clear time difference in all events. Finally, we get 24 proton injections and 17 electron injections at GOES-14.

Figure 8a shows the local time dependence of the proton injections and that of the electron injections. The proton injections have occurrence peak near the 22 MLT meridian (the average is 21.8 MLT), while the electron injections have occurrence peak near the 23 MLT meridian (the average is 22.5 MLT). This is reasonable, since protons drift westward and electrons drift eastward, and is consistent with the previous statistical results (e.g., Erickson et al., 1979; Sauvaud & Winckler, 1980).

4.1. Average Variations of Magnetic Field, Electron Flux, and Proton Flux

To investigate the relationship of particle behavior to the current wedge, we select events where the center of the current wedge is located near the GOES-14 meridian. As seen in section 3.1, we observe both proton and electron injections near the center of the current wedge. We have five simultaneous proton and electron injections plus three proton injections in which 100–200-keV electron flux increases (although electron increases do not meet the adopted criteria). The local time dependence of the selected eight events are presented in Figure 8a. The events are distributed in 20–22 MLT, and the average value is 21.5 MLT.

Superposed epoch analyses are used to investigate representative characteristics of the particle injection events. Zero epoch is defined as the time of a rapid flux increase in the 80–110-keV proton flux (time resolution of 16 s) at GOES-14. The magnetic field data are averaged for 2.05 s (four data points). Any other timing (e.g., start time of *D* deflection) cannot be determined unambiguously for all events. Figure 9 presents the average variations for the period of −10 to +20 min of the epoch time at GOES-15 (19.5 MLT at zero epoch), GOES-14 (21.5 MLT), and GOES-13 (23.5 MLT), although we had examined the average variations using 1-min averaged data for the period of −120 to +120 min. We focus on the robust characteristics of variations near the zero epoch to confirm the findings of the event studies described in section 3.

We first examine the average magnetic field behavior at three MLT positions. The negative *D* deflection at GOES-13 starts 1 or 2 min before the zero epoch. The first signal of the onset of a substorm is detected as the *D* deflection caused by the field-aligned current of the current wedge in any local time position (e.g., Nagai, 1982b), and the effects of the field-aligned currents are usually large at high latitudes. The definition of zero epoch using the particle behavior may cause this result, although it has no significant effect on the present analysis. GOES-15 observes a small positive *D* deflection. GOES-14 shows a spike-like positive and then negative variations. A rapid dipolarization is seen at GOES-14. At GOES-13, the magnetic field shows a more gradual dipolarization. GOES-15 shows further decreases in magnetic field intensity and field inclination after the zero epoch. These variations at the three different MLT positions are consistent with average magnetic field variations obtained using GOES-5 and GOES-6 for 194 substorms by Nagai (1991) and the observations in the event studies in section 3. A sharp proton flux increase is seen at GOES 14, and a proton flux enhancement continues for less than 5 min. The electron flux increase is gradual even at GOES-14. The proton flux does not show any increase just after the zero epoch, and its increase around +6 min is associated with a local dipolarization in the magnetic field at GOES-13. The electron flux shows a decrease in association with a depression in the magnetic field intensity at GOES-15. The proton flux increase is slightly delayed and is gradual at GOES-15.

Since only eight events are available in this procedure, we make similar analyses with the GOES-14 and GOES-15 pair adding the data obtained in 2018. We can get 21 simultaneous proton and electron injection events at GOES-15 using the same selection method. The local time dependence of the selected events is presented in Figure 8b, and the average occurrence local time is 21.9 MLT. Figure 10 shows the average variations in the magnetic field, the electron fluxes, and the proton fluxes. Twelve events in 2016–2017 are used for making the average variations at GOES-13. A sharp dipolarization within 5 min is evident with a positive *D* deflection at GOES-15. A dipolarization in the magnetic field is delayed with 3 min at GOES-14 (00 MLT) and at 10 min at GOES-13 (02 MLT). The proton flux reaches its peak within 1 min and the proton enhancement continues for less than 10 min at GOES-15. The proton flux variations are attributable to adiabatic response to the magnetic field variations at GOES-14 and GOES-13. The electron flux shows a gradual increase in comparison with the proton flux at GOES-15. A flux decrease after the zero epoch is seen in higher-energy electron channels at GOES-14 and GOES-13, and these are signatures of drifting holes. Energy dispersion is evident in the electron fluxes at GOES-14 and GOES-13. Hence, the results at GOES-15 (Figure 10) are consistent with those at GOES-14 (Figure 9) and the findings in section 3.

4.2. Electron Injections

Figure 11 shows the average variations for the 17 electron injection events at GOES-14 (at 22.5 MLT), using 1-min averaged data. Although the start time of the flux increase is defined with the 100–200-keV electron data, electrons with the whole energy range (30–600 keV) start to increase almost simultaneously. The dipolarization in the magnetic field with a negative *D* deflection also starts simultaneously. The proton flux starts to increase. Since it reaches only to the preevent flux level (at −120 min), the proton flux variation should be attributed the adiabatic response to the magnetic field variation. At GOES-13 (at 00.5 MLT), the electron flux increases are delayed by 2 min and lower energy electron fluxes increase more gradually. At GOES-15 (at 20.5 MLT), the proton flux increase starts at zero epoch and has a clear enhancement, and any electron flux injection is not discernible. Hence, GOES-15, which is located at 2-hr earlier local time, is located west of the central current wedge.

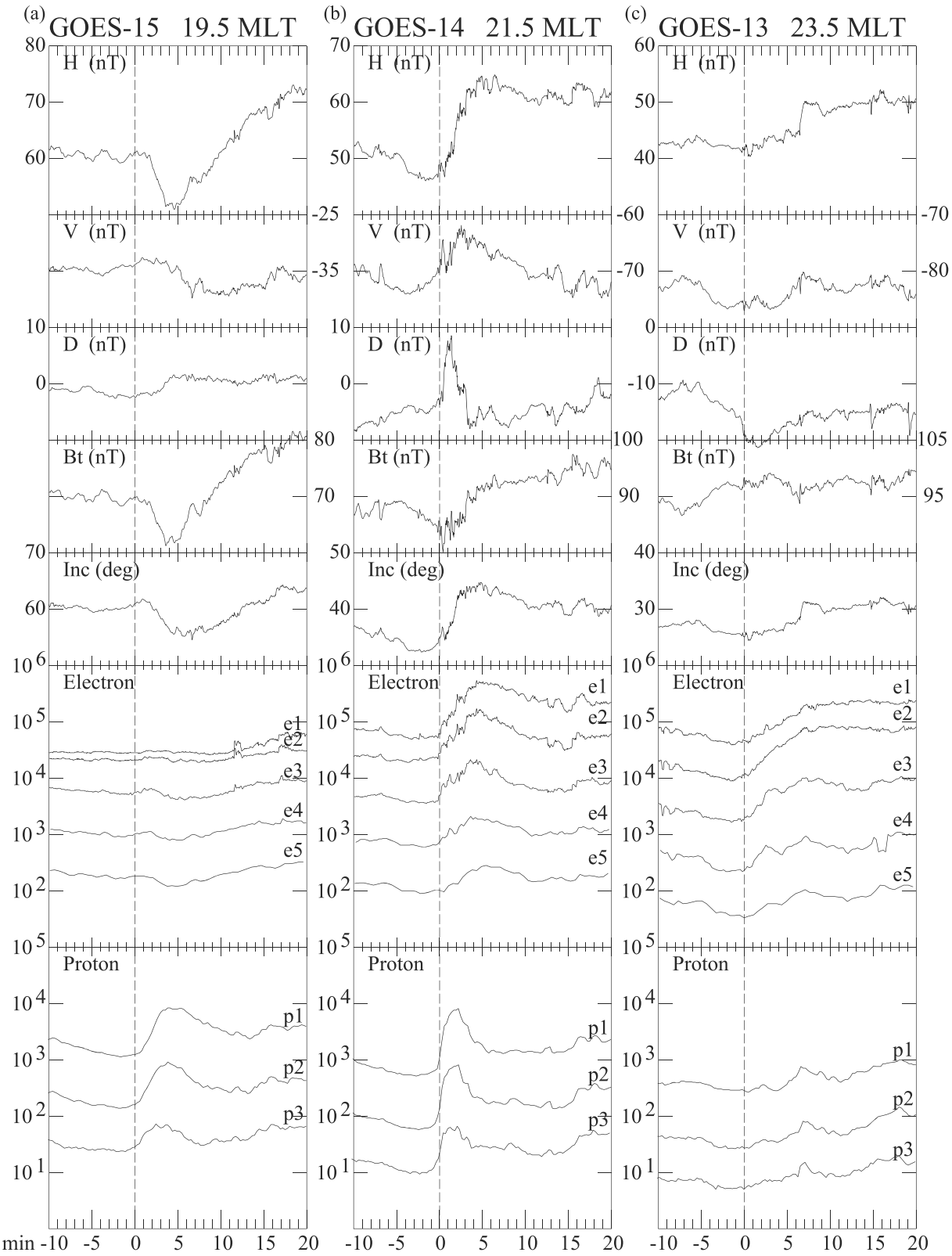

Figure 9. Average magnetic field, electron flux, and proton flux variations for nine injection events at the (a) GOES-15, (b) GOES-14, and (c) GOES-13 positions. The zero epoch is the timing of the rapid proton flux increase at GOES-14. The variations for the period of −10 to +20 min are presented. Particle flux unit is $cm^{-2}{\cdot}s^{-1}{\cdot}sr^{-1}{\cdot}keV^{-1}$.

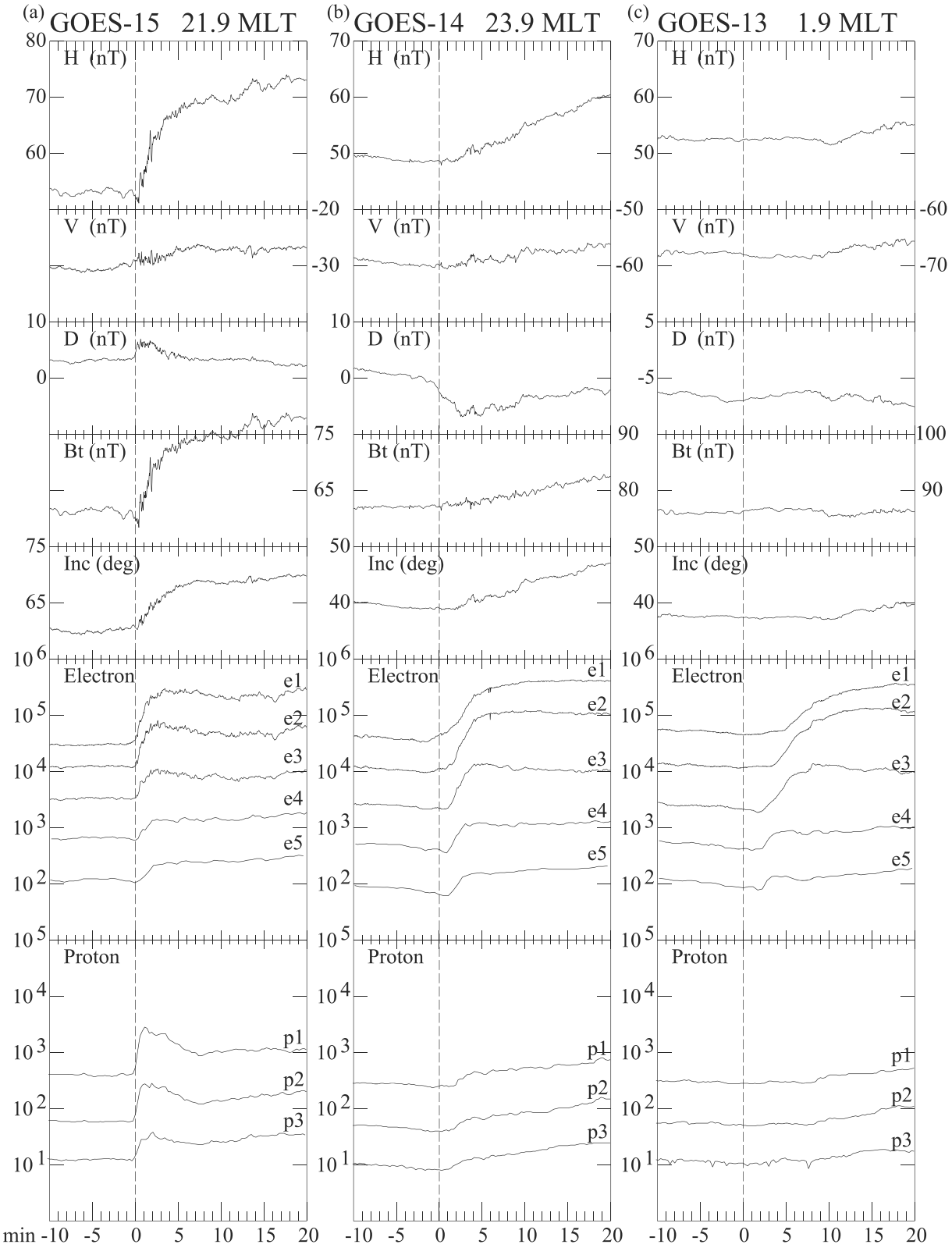

Figure 10. Average magnetic field, electron flux, and proton flux variations for 21 injection events at the (a) GOES-15, (b) GOES-14, and (c) GOES-13 positions. The zero epoch is the timing of the rapid proton increase at GOES-15. The variations for the period of −10 to +20 min are presented. Particle flux unit is cm $^{-2}$·s^{-1}·sr^{-1}·keV^{-1}.

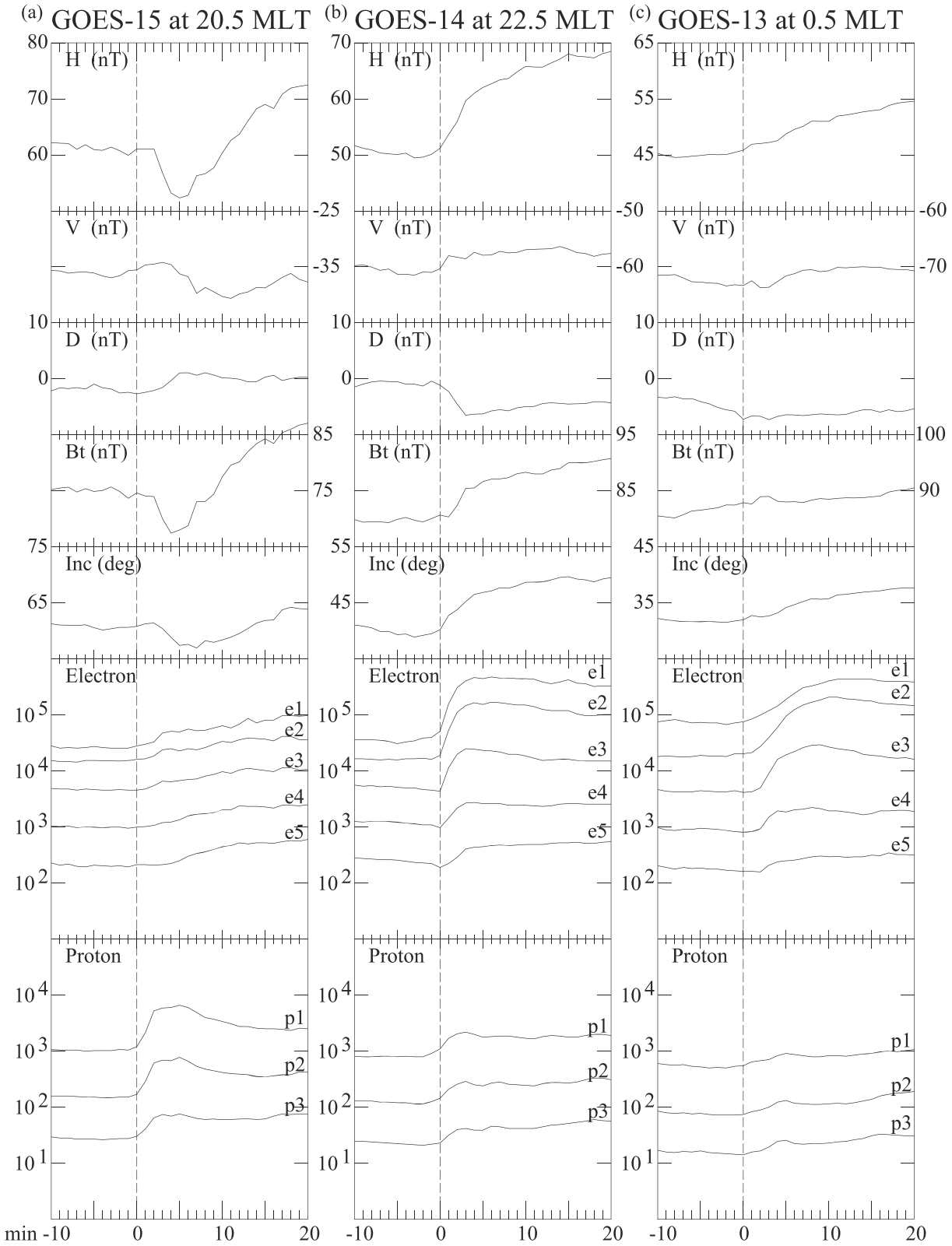

Figure 11. Average magnetic field, electron flux, and proton flux variations for 17 events at the (a) GOES-15, (b) GOES-14, and (c) GOES-13 positions. The zero epoch is the timing of the rapid electron flux increase at GOES-14. The variations for the period of −10 to +20 min are presented. Particle flux unit is $cm^{-2}{\cdot}s^{-1}{\cdot}sr^{-1}{\cdot}keV^{-1}$.

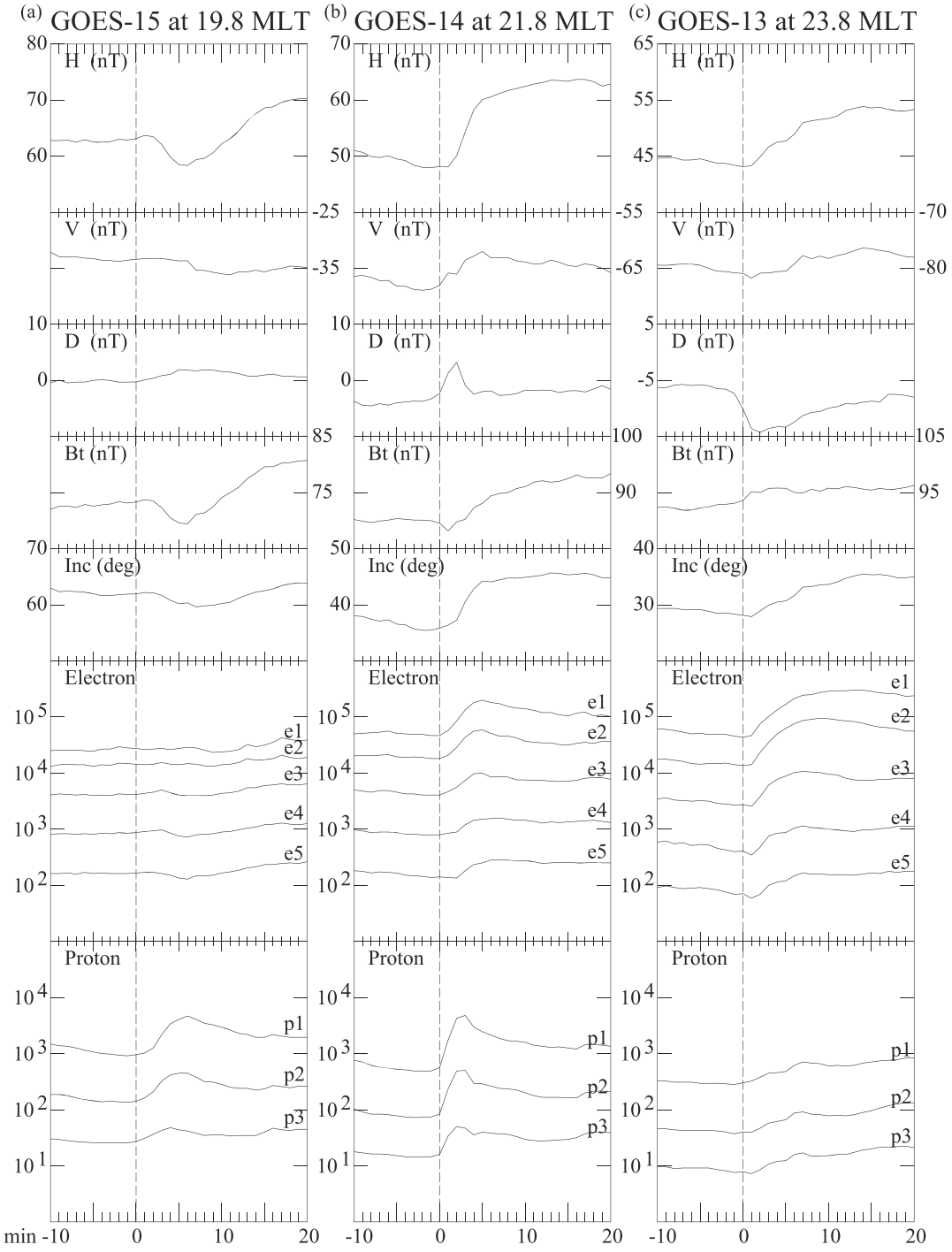

Figure 12. Average magnetic field, electron flux, and proton flux variations for 24 events at the (a) GOES-15, (b) GOES-14, and (c) GOES-13 positions. The zero epoch is the timing of the rapid proton flux increase at GOES-14. The variations for the period of −10 to +20 min are presented. Particle flux unit is $cm^{-2}{\cdot}s^{-1}{\cdot}sr^{-1}{\cdot}keV^{-1}$.

4.3. Proton Injections

Figure 12 shows the average variations for the 24 proton injection events at GOES-14 (at 21.8 MLT), using 1-min averaged data. The zero epoch is defined with the 80–110-keV proton data. A positive *D* deflection starts at the zero epoch. The electron flux increases with a slight delay (2 min) at GOES-13 (23.8 MLT),

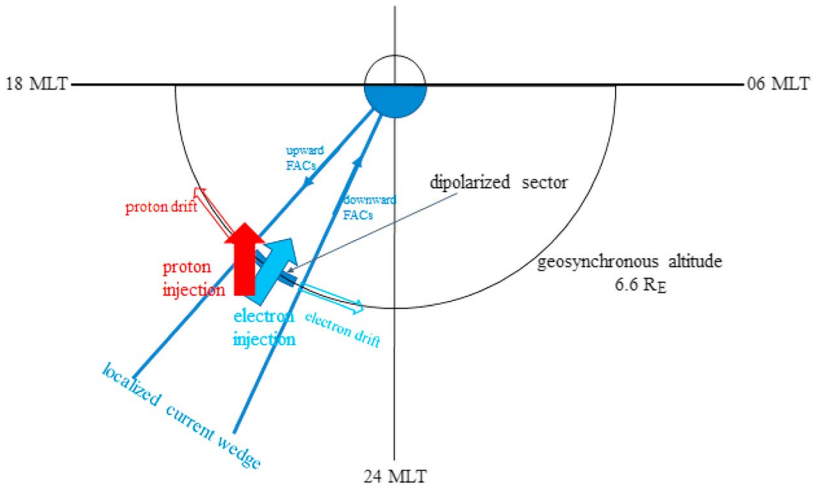

Figure 13. Schematic of the relationship among proton injection, electron injection, and a current wedge.

while the proton flux increases with a slight delay (2 min) at GOES-15 (at 19.8 MLT). These particle behaviors indicate the localization of injection processes near the GOES-14 meridian.

5. Summary and Discussion

Particle injection is an important process for providing new particle populations in the outer radiation belt of the inner magnetosphere. In quasi-steady convection, energetic particles cannot be directly supplied from the plasma sheet. Even with an enhanced convection electric field, energetic (tens to hundreds of keV) protons and electrons are diverted by the dipolar magnetic field and transported toward the dayside magnetopause. An importance of substorm-associated magnetic and electric fields is emphasized even beyond 6.6 R_E (e.g., Gabrielse et al., 2016, 2017; Ganushkina et al., 2013). Here we are interested in the supply of particle population into the radiation belts and ring current region ($L < 6.6$) of the inner magnetosphere. Since particles should cross the geosynchronous altitude somewhere, we seek a possible "path" in which these particles are transported. In the previous studies described in section 1, the exact location of the path and its width are not fully known, as particle behaviors are mainly discussed only on the basis of particle data, not using the simultaneous magnetic field data. It is possible that a so-called "dispersionless injection" is caused by the particle trapping boundary motion in some cases. The particle trapping boundary motion is a redistribution of particle population, which moves outward rather than inward during substorms at geosynchronous orbit.

This study confirms that energetic particle injection processes are tightly coupled with configuration changes in the magnetic field, which are well represented by the current wedge. The current wedge at geosynchronous altitude is usually not a global phenomenon for moderate substorms, and the evolution of the current wedge produces highly localized particle and field changes. One sign of current wedge initiation is the effect of field-aligned currents, and the current wedge forms initially in a narrow local time sector. A main result found in this study is that particle injection only takes place in the center of the current wedge for moderate substorms, as illustrated in Figure 13. The center of the current wedge is usually located at 21–22 MLT. Protons and electrons can be injected, although there are often time delays between a proton flux increase and an electron flux increase. The electron flux increase is tightly coupled with local dipolarization in the magnetic field. In the initial stage of current wedge evolution, the field is still not dipolarized and remains taillike, even near the central region of the current wedge. Protons can be injected before local dipolarization in the magnetic field, as seen in the events described in sections 3.2–3.4, and proton injection likely starts at the time of current wedge initiation. A 100-keV proton has a Larmor radius of approximately 440 km in the magnetic field of 100 nT. The energetic protons likely intrude on geosynchronous altitude. Energetic electrons having a much smaller Larmor radius are probably transported with some time delays.

At the position 2 hr east of the center of the current wedge, electron flux increases are attributable to the appearance of drifting electrons, which intrude on geosynchronous altitude in the center of the current wedge. A typical delay time is less than 2 min, but the delay is evident, and drifting holes and energy dispersion can be found. Electrons with energies <100 keV show flux enhancements for a fairly long duration. This indicates that the inner edge of the plasma sheet reaches geosynchronous altitude and stays there, and the plasma sheet can supply these lower energy (<100 keV) electrons. Flux enhancements in electrons with energies >100 keV can be observed in the event studies, but the flux enhancements are transient.

At the position 2 hr west of the center of the current wedge, proton flux increases are attributable to the appearance of drifting protons, which are injected at geosynchronous altitude in the center of the current wedge. In this MLT sector, no local dipolarization takes place in the magnetic field. For the average current wedge, the western edge of the current wedge is located in the 2030 MLT meridian (Nagai, 1991). Electrons show variations associated with the changes in magnetic field intensity.

Proton injection is likely a process with a duration of 5 min. In the superposed epoch analysis, a rapid field change continues for only 3 min at the center of the current wedge (at GOES-14 or GOES 15), as seen in Figures 9 and 10. The magnetic field intensity increases in the same time scale. It is likely that the intense induction electric field is generated only with this time scale. This electric field results in particle injection at geosynchronous altitude, although the induction electric field during dipolarization is not fully examined (e.g., Aggson et al., 1983). It is likely that high-energy electron injection occurs in similar time scales. The population of electrons with energies >100 keV is small in the plasma sheet, so that injection processes can be discriminated by the earthward shift of the inner edge of the plasma sheet. The injection and earthward shift of the plasma sheet may occur simultaneously. Injections of electrons with energies >100 keV are not easily examined in the wide-energy channel data. Therefore, injections of electrons with energies >100 keV should be examined with instruments having higher-energy resolutions.

Thomsen et al. (2001) reported with the two-spacecraft observations that the ion and electron injection regions are spatially offset in the azimuthal direction. Although their results are based on the observations with lower time resolution (>60 s) without any simultaneous magnetic field measurements, their results are consistent with the present results. They also reported the expansion of the injection region azimuthally. However, we do not find any azimuthal expansion of the injection region for high-energy (>100 keV) protons and electrons. Appearance of the plasma sheet electrons (with energies of <100 keV) is associated with local dipolarization in the magnetic field in this study. Since the local dipolarization region expands azimuthally eastward and westward, the injection region for low-energy protons and electrons may expand. However, any possibility that apparent particle injections are caused by the particle trapping boundary motion cannot be eliminated without 3-D particle measurements with high time resolution. Gabrielse et al. (2014, 2016, 2017) have examined particle dynamics mainly beyond the geosynchronous altitude using the data from the Time History of Events and Macroscale Interactions during Substorms spacecraft. They show the spatial distributions of dispersionless injection events at $R > 12\ R_E$ and $R < 12\ R_E$. The spatial distributions for ions and electrons are rather similar at $R > 12\ R_E$. At $R < 12\ R_E$, the occurrence peak shifts slightly to earlier MLTs for ions and to the later MLTs for electrons. Malykhin et al. (2018) have found the difference between proton behavior and electron behavior near 9 R_E in the postmidnight region. It is possible that the diversion between ions and electrons can occur well beyond geosynchronous orbit. This is consistent with the present result. Motoba et al. (2018) recently examined ion injections inside geosynchronous altitude, and also found that particle behavior is strongly governed by changes in the magnetic field.

6. Conclusions

Using tens to hundreds of keV proton and electron measurements and simultaneous magnetic field measurements from three Geostationary Operational Environmental Satellites [GOES-13 (75°W), GOES-14 (105°W), and GOES-15 (135°W)], we investigated proton and electron injections and their relationship to the current wedge at geosynchronous altitude. Rapid flux increases in protons and electrons are selected on the nightside. The current wedge is identified with dipolarization in the magnetic field. The central meridian of the current wedge is determined from variations in the east-west component (D) of the magnetic field. Proton and electron injection processes are localized within the central region of the current wedge for

moderate substorms, the width of which is less than 2 hr in local time. The center of the current wedge usually forms in the premidnight sector. It is likely that proton injections take place only under the western upward field-aligned currents of the current wedge. Proton injections are closely related to the formation of the current wedge at geosynchronous orbit, and thus the onset of a substorm, usually before local dipolarization in the magnetic field. Proton injection in the energy range of 80–110 keV continues only for 5 min, suggesting that the particle injection has the time scale of 5 min at geosynchronous altitude. Electron injections in the energy rage of <100 keV are tightly coupled with local dipolarization in the magnetic field, and these take place mostly in the center of the current wedge.

Acknowledgments
The NOAA data are obtained from NOAA National Centers for Environmental Information (http://www.ngdc.noaa.gov/stp/satellite/goes/index.html) and the NASA/CDAWeb (http://cdaweb.gsfc.nasa.gov). The ground magnetic field data and geomagnetic indices are provided by the World Data Center for Geomagnetism at Kyoto University (http://wdc.kugi.kyoto-u.ac.jp/index.html) and the THEMIS website (http://themis.ssl.berkeley.edu/index.shtml). The work of TN at ISAS/JAXA is supported by MEXT/JSPS KAKENHI grant 17H06140.

References

Aggson, T. L., Heppner, J. P., & Maynard, N. C. (1983). Observations of large magnetospheric electric fields during the onset phase of a substorm. *Journal of Geophysical Research*, *88*(A5), 3981–3990. https://doi.org/10.1029/JA088iA05p03981

Arnoldy, R. L., & Moore, T. E. (1983). Longitudinal structure of substorm injections at synchronous orbit. *Journal of Geophysical Research*, *83*(A8), 6213–6220. https://doi.org/10.1029/JA088iA08p06213

Bogott, F. H., & Mozer, F. S. (1973a). ATS 5 observations of energetic proton injection. *Journal of Geophysical Research*, *78*(34), 8113–8118. https://doi.org/10.1029/JA078i034p08113

Bogott, F. H., & Mozer, F. S. (1973b). Nightside energetic particle decreases at the synchronous orbit. *Journal of Geophysical Research*, *78*(34), 8119–8127. https://doi.org/10.1029/JA078i034p08119

Clauer, C. R., & McPherron, R. L. (1974). Mapping the local time-universal time development of magnetospheric substorms using mid-latitude magnetic observations. *Journal of Geophysical Research*, *79*(19), 2811–2820. https://doi.org/10.1029/JA079i019p02811

Coleman, P. J. Jr., & McPherron, R. L. (1970). Fluctuations in the distant geomagnetic field during substorms: ATS 1. In B. M. McCormac (Ed.), *Particles and Fields in the Magnetosphere* (p. 171–194). Hingham, MA: D. Reidel.

Coleman, P. J. Jr., & McPherron, R. L. (1976). Substorm observations of magnetic perturbations and ULF waves at synchronous orbit by ATS-1 and ATS-6. In K. Knott & B. Battrick (Eds.), *The Scientific Satellite Programme During the International Magnetospheric Study* (p. 345–365). Hingham, MA: D. Reidel.

Cummings, W. D., Barfield, J. N., & Coleman, P. J. Jr. (1968). Magnetospheric substorms observed at the synchronous orbit. *Journal of Geophysical Research*, *73*(21), 6687–6698. https://doi.org/10.1029/JA073i021p06687

Cummings, W. D., & Coleman, P. J. Jr. (1968). Simultaneous magnetic field variations at the Earth's surface and at synchronous, equatorial distance, 1, Bay-associated events. *Radio Science*, *3*(7), 758–761. https://doi.org/10.1002/rds196837758

DeForest, S. E., & McIlwain, C. E. (1971). Plasma clouds in the magnetosphere. *Journal of Geophysical Research*, *76*(16), 3587–3611. https://doi.org/10.1029/JA076i016p03587

Erickson, K. N., Swanson, R. L., Walker, R. J., & Winckler, J. R. (1979). A study of magnetosphere dynamics during auroral electrojet events by observations of energetic electron intensity changes at synchronous orbit. *Journal of Geophysical Research*, *84*(A3), 931. https://doi.org/10.1029/JA084iA03p00931

Erickson, K. N., & Winckler, J. R. (1973). Auroral electrojets and evening sector electron dropouts at synchronous orbit. *Journal of Geophysical Research*, *78*(34), 8373–8380. https://doi.org/10.1029/JA078i034p08373

Fairfield, D. H., Acuna, M. H., Zanetti, L. J., & Potemra, T. A. (1987). The magnetic field of the equatorial magnetotail: AMPTE/CCE observations at $R < 8.8\ R_E$. *Journal of Geophysical Research*, *92*(A7), 7432–7444. https://doi.org/10.1029/JA092iA07p07432

Friedel, R. H. W., Korth, A., & Kremser, G. (1996). Substorm onsets observed by CRRES: Determination of energetic particle source regions. *Journal of Geophysical Research*, *101*(A6), 13,137–13,154. https://doi.org/10.1029/96JA00399

Gabrielse, C., Angelopoulos, V., Harris, C., Artemyev, A., Kepko, L., & Runov, A. (2017). Extensive electron transport and energization via multiple, localized dipolarizing flux bundles. *Journal of Geophysical Research: Space Physics*, *122*, 5059–5076. https://doi.org/10.1002/2017JA023981

Gabrielse, C., Angelopoulos, V., Runov, A., & Turner, D. L. (2014). Statistical characteristics of particle injections throughout the equatorial magnetotail. *Journal of Geophysical Research: Space Physics*, *119*, 512–2,535. https://doi.org/10.1002/2013JA019638

Gabrielse, C., Harris, C., Angelopoulos, V., Artemyev, A., & Runov, A. (2016). The role of localized inductive electric fields in electron injections around dipolarizing flux bundles. *Journal of Geophysical Research: Space Physics*, *121*, 9560–9585. https://doi.org/10.1002/2016JA023061

Ganushkina, N. Y., Amariutei, O., Shprits, Y. Y., & Liemohn, M. (2013). Transport of the plasma sheet electrons to the geostationary distances. *Journal of Geophysical Research: Space Physics*, *118*, 82–98. https://doi.org/10.1029/2012JA017923

Gelpi, C., Hughes, W. J., Singer, H. J., & Lester, M. (1985). Mid-latitude Pi 2 polarization pattern and synchronous orbit magnetic activity. *Journal of Geophysical Research*, *90*(A7), 6451. https://doi.org/10.1029/JA090iA07p06451

Jaynes, A. N., Lessard, M. R., Rodriguez, J. V., Donovan, E., Loto'aniu, T. M., & Rychert, K. (2013). Pulsating auroral electron flux modulations in the equatorial magnetosphere. *Journal of Geophysical Research: Space Physics*, *118*, 4884–4894. https://doi.org/10.1002/jgra.50434

Kivelson, M., & Russell, C. T. (1995). *Introduction of Space Physics*. Cambridge: Cambridge University Press.

Kokubun, S., & McPherron, R. L. (1981). Substorm signatures at synchronous altitude. *Journal of Geophysical Research*, *86*(A13), 11,265. https://doi.org/10.1029/JA086iA13p11265

Lezniak, T. W., & Winckler, J. R. (1970). Experimental study of magnetospheric motions and the energetic electrons during substorms. *Journal of Geophysical Research*, *75*(34), 7075–7098. https://doi.org/10.1029/JA075i034p07075

Malykhin, A. Y., Grigorenko, E. E., Kronberg, E. A., Koleva, R., Ganushkin, N. Y., Kozak, L., & Daly, P. W. (2018). Contrasting dynamics of electrons and protons in the near-Earth plasma sheet during dipolarization. *Annales Geophysicae*, *36*(3), 741–760. https://doi.org/10.5194/angeo-36-741-2018

McPherron, R. L., & Barfield, J. N. (1980). A seasonal change in the effect of field-aligned currents at synchronous orbit. *Journal of Geophysical Research*, *85*(A12), 6743. https://doi.org/10.1029/JA085iA12p06743

McPherron, R. L., Russell, C. T., & Aubry, M. P. (1973). Satellite studies of magnetospheric substorms on August 15, 1968, 9, Phenomenological model for substorms. *Journal of Geophysical Research*, *78*(16), 3131–3149. https://doi.org/10.1029/JA078i016p03131

Motoba, T., Ohtani, S., Gkioulidou, M., Ukhorskiy, A., Mitchell, D. G., Takahashi, K., et al. (2018). Response of different ion species to local magnetic dipolarization inside geosynchronous orbit. *Journal of Geophysical Research: Space Physics*, *123*, 5420–5234. https://doi.org/10.1029/2018JA025557

Nagai, D., Baker, N., & Higbie, P. R. (1983). Development of substorm activity in multiple-onset substorms at synchronous orbit. *Journal of Geophysical Research*, *88*(A9), 6994–7004. https://doi.org/10.1029/JA088iA09p06994

Nagai, T. (1982a). Local time dependence of electron flux changes during substorms derived from multi-satellite observation at synchronous orbit. *Journal of Geophysical Research*, *87*(A5), 3456–3468. https://doi.org/10.1029/JA087iA05p03456

Nagai, T. (1982b). Observed magnetic substorm signatures at synchronous altitude. *Journal of Geophysical Research*, *87*(A6), 4405–4417. https://doi.org/10.1029/JA087iA06p04405

Nagai, T. (1987). Field-aligned currents associated with substorms in the vicinity of synchronous orbit, 2. GOES 2 and GOES 3 observations. *Journal of Geophysical Research*, *92*(A3), 2432–2446. https://doi.org/10.1029/JA092iA03p02432

Nagai, T. (1991). An empirical model of substorm-related magnetic field variations at synchronous orbit. In J. R. Kan, T. A. Potemra, S. Kokubun, & T. Iijima (Eds.), *Magnetospheric Substorms* (pp. 91–95). Washington, DC: American Geophysical Union.

Nagai, T., Singer, H. J., Ledley, B. G., & Olsen, R. C. (1987). Field-aligned currents associated with substorms in the vicinity of synchronous orbit, 1. The July 5, 1979, substorm observed by SCATHA, GOES 3, and GOES 2. *Journal of Geophysical Research*, *92*(A3), 2425–2431. https://doi.org/10.1029/JA092iA03p02425

Nagai, T., Takahashi, K., Potemra, T. A., McEntire, R. W., Lopez, R. E., & Klumpar, D. M. (1990). The structure of the Birkeland current system in the post-midnight plasma sheet. *Geophysical Research Letters*, *17*(8), 1057–1060. https://doi.org/10.1029/GL017i008p01057

Sauvaud, J.-A., & Winckler, J. R. (1980). Dynamics of plasma, energetic particles, and fields near synchronous orbit in the nighttime sector during magnetospheric substorms. *Journal of Geophysical Research*, *85*(A5), 2043. https://doi.org/10.1029/JA085iA05p02043

Sergeev, V., Shukhtina, M. A., Rasinkangas, R., Korth, A., Reeves, G. D., Singer, H. J., et al. (1998). Event study of deep energetic particle injections during substorm. *Journal of Geophysical Research*, *103*(A5), 9217–9234. https://doi.org/10.1029/97JA03686

Sergeev, V. A., Bösinger, T., Belian, R. D., Reeves, G. D., & Cayton, T. E. (1992). Drifting holes in the energetic electron flux at geosynchronous orbit following substorm onset. *Journal of Geophysical Research*, *97*(A5), 6541–6548. https://doi.org/10.1029/92JA00182

Singer, H. J., Hughes, W. J., Gelpi, C., & Ledley, B. G. (1985). Magnetic disturbances in the vicinity of the synchronous orbit and the substorm current wedge: A case study. *Journal of Geophysical Research*, *90*(A10), 9583. https://doi.org/10.1029/JA090iA10p09583

Singer, H. J., Matheson, L., Grubb, R., Newman, A., & Bouwer, D. (1996). Monitoring space weather with the GOES magnetometers. In E. Washwell (Ed.), *GOES-8 and beyond* (Vol. 2812, pp. 299–308). Boulder, CO: NOAA Space Environment Center. https://doi.org/10.1117/12.254077

Tang, C. L., Xie, X. J., Ni, B., Su, Z. P., Reeves, G. D., Zhang, J.-C., et al. (2018). Rapid enhancements of the seed populations in the heart of the Earth's outer radiation belt: A multicase study. *Journal of Geophysical Research: Space Physics*, *123*, 4895–4907. https://doi.org/10.1029/2017JA025142

Thomsen, M. F., Birn, J., Borovsky, J. E., Morzinski, K., McComas, D. J., & Reeves, G. D. (2001). Two satellite observations of substorm injections at geosynchronous orbit. *Journal of Geophysical Research*, *106*(A5), 8405–8416. https://doi.org/10.1029/2000JA000080

Turner, D. L., Claudepierre, S. G., Fennell, J. F., O'Brien, T. P., Blake, J. B., Lemon, C., et al. (2015). Energetic electron injections deep into the inner magnetosphere associated with substorm activity. *Geophysical Research Letters*, *42*, 2079–2087. https://doi.org/10.1002/2015GL063225

Walker, R. J., Erickson, K. N., Swanson, R. L., & Winckler, J. R. (1976). Substorm-associated particle boundary motion at synchronous orbit. *Journal of Geophysical Research*, *81*(31), 5541–5550. https://doi.org/10.1029/JA081i031p05541